S-nitrosoglutathione reductase–dependent PPARγ denitrosylation participates in MSC-derived adipogenesis and osteogenesis

Yenong Cao,[1,2] Samirah A. Gomes,[1] Erika B. Rangel,[1] Ellena C. Paulino,[1] Tatiana L. Fonseca,[3] Jinliang Li,[1,4,5] Marilia B. Teixeira,[6] Cecilia H. Gouveia,[6] Antonio C. Bianco,[3] Michael S. Kapiloff,[1,4,5,7] Wayne Balkan,[1,7] and Joshua M. Hare[1,2,7]

[1]Interdisciplinary Stem Cell Institute, [2]Department of Molecular and Cellular Pharmacology, [3]Division of Endocrinology, Diabetes and Metabolism, [4]Department of Pediatrics, and [5]Cardiac Signal Transduction and Cellular Biology Laboratory, Miller School of Medicine, University of Miami, Miami, Florida, USA. [6]Department of Anatomy, Institute of Biomedical Sciences, University of São Paulo, São Paulo, Brazil. [7]Department of Medicine, Miller School of Medicine, University of Miami, Miami, Florida, USA.

Bone marrow–derived mesenchymal stem cells (MSCs) are a common precursor of both adipocytes and osteoblasts. While it is appreciated that PPARγ regulates the balance between adipogenesis and osteogenesis, the roles of additional regulators of this process remain controversial. Here, we show that MSCs isolated from mice lacking S-nitrosoglutathione reductase, a denitrosylase that regulates protein S-nitrosylation, exhibited decreased adipogenesis and increased osteoblastogenesis compared with WT MSCs. Consistent with this cellular phenotype, S-nitrosoglutathione reductase–deficient mice were smaller, with reduced fat mass and increased bone formation that was accompanied by elevated bone resorption. WT and S-nitrosoglutathione reductase–deficient MSCs exhibited equivalent PPARγ expression; however, S-nitrosylation of PPARγ was elevated in S-nitrosoglutathione reductase–deficient MSCs, diminishing binding to its downstream target fatty acid–binding protein 4 (FABP4). We further identified Cys 139 of PPARγ as an S-nitrosylation site and demonstrated that S-nitrosylation of PPARγ inhibits its transcriptional activity, suggesting a feedback regulation of PPARγ transcriptional activity by NO-mediated S-nitrosylation. Together, these results reveal that S-nitrosoglutathione reductase–dependent modification of PPARγ alters the balance between adipocyte and osteoblast differentiation and provides checkpoint regulation of the lineage bifurcation of these 2 lineages. Moreover, these findings provide pathophysiological and therapeutic insights regarding MSC participation in adipogenesis and osteogenesis.

Introduction

Bone marrow–derived mesenchymal stem cells (MSCs) are multipotent stem cells with the capacity to self renew and differentiate into mesodermal lineages that include adipocytes, osteoblasts, and chondrocytes (1, 2). Disrupting the balance between adipocyte and osteoblast differentiation with enhanced adipogenesis underlies the adaptations of aging (3, 4) and numerous bone and metabolic diseases, including osteoporosis (5). Distorting this balance by increasing osteogenesis leads to progressive osseous heteroplasia, characterized by ectopic bone formation (6). Nevertheless, the regulation of MSC lineage bifurcation into adipocytes and osteoblasts remains poorly understood, and in this regard, PPARγ is a prominent regulatory candidate (7, 8).

PPARγ belongs to the nuclear receptor family of ligand-inducible transcription factors. As a key regulator of both adipogenesis and osteogenesis, PPARγ is controlled at both transcriptional and translational levels. Upon ligand binding, PPARγ undergoes conformational changes and recruits multiple cofactors, leading to the activation of its target genes. Another layer of control over PPARγ involves posttranslational modifications. Bone marrow cells from mice with *Pparg* haploinsufficiency have diminished adipogenic differentiation capacity and increased osteogenesis (7). However, the role of potential regulators of PPARγ activity in this differentiation shift remains unknown.

One potential regulator is nitric oxide (NO), which is synthesized by 3 isoforms of NO synthases (NOSs), neuronal (nNOS, NOS1), inducible (iNOS, NOS2), and endothelial NOS (eNOS, NOS3). NO enhances adipogenesis of human preadipocytes while decreasing their proliferation (9). Adipogenic differentiation of mesenchymal cells is also inhibited by the suppression of NO production (10). In addition, NO is a crucial regulator of osteoblast proliferation and differentiation. Studies in mice with a targeted deletion of *Nos1*, *Nos2*, or *Nos3* show a manifestation of distinct bone effects. *Nos1*$^{-/-}$ mice have higher bone mass with decreased bone remodeling but normal osteoblast proliferation or differentiation, suggesting a non–cell-autonomous mechanism (11). NOS2 modulates cytokine secretion and thereby affects osteoblast differentiation (12). Osteoblasts from *Nos3*$^{-/-}$ mice have lower proliferation and alkaline phosphatase expression, consistent with decreased bone mass (13). These observations suggest that NO plays an important role in regulating the balance between adipocyte and osteoblast differentiation.

NO bioactivity is based not only on production by NOSs, but also by protein S-nitrosylation, a posttranslational modification

Conflict of interest: Joshua M. Hare reports having a patent for cardiac cell–based therapy, receiving research support from BioCardia, having equity in Kardia, and having a relationship with Vestion Corp. that includes equity, board membership, and consulting. None of these entities contributed funding to this study.
Submitted: July 23, 2014; **Accepted:** February 6, 2015.
Reference information: *J Clin Invest*. 2015;125(4):1679–1691. doi:10.1172/JCI73780.

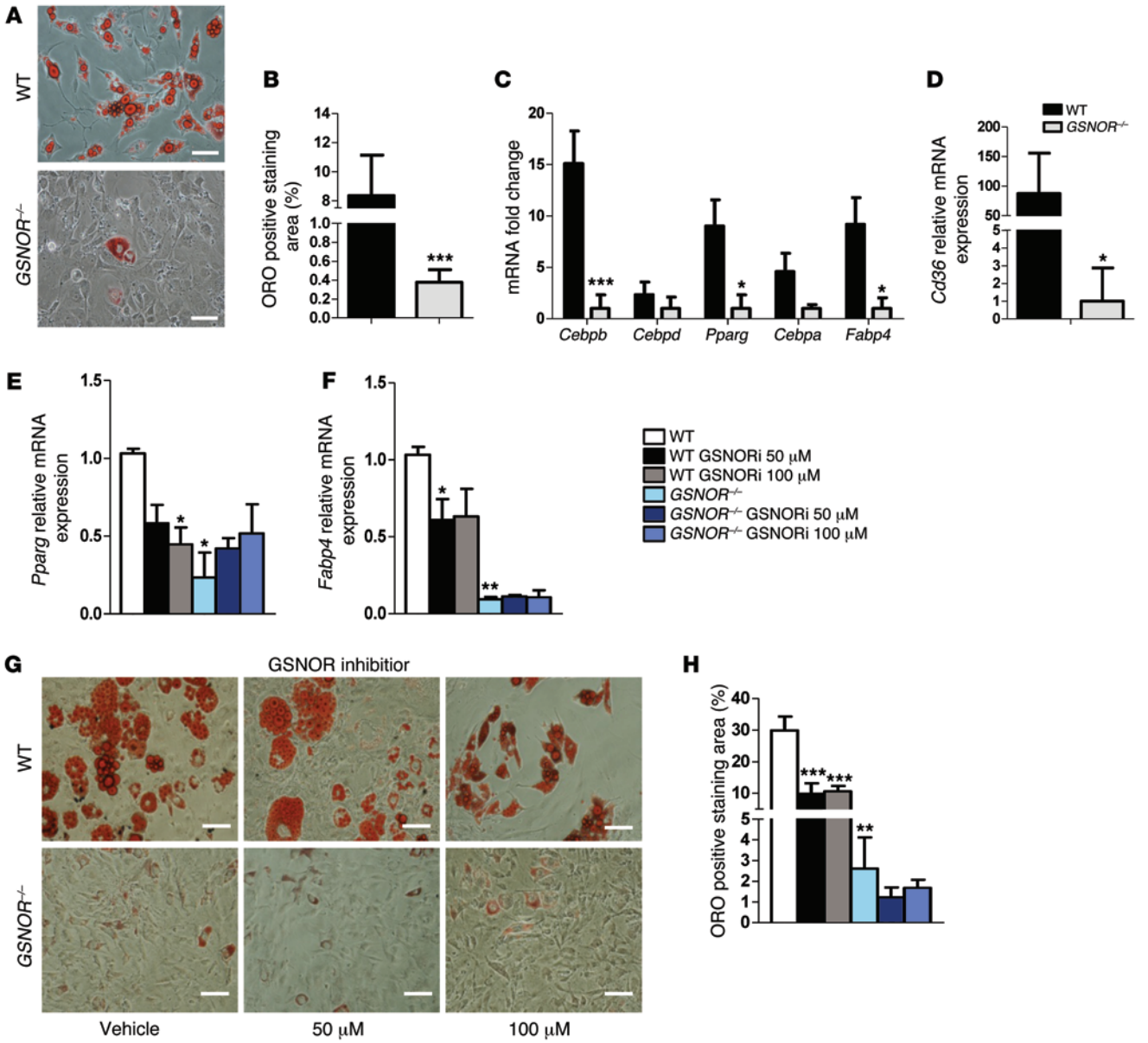

Figure 1. *GSNOR*$^{-/-}$ MSCs have impaired adipogenic differentiation. (**A**) ORO staining of WT and *GSNOR*$^{-/-}$ cells. Scale bars: 100 μm. $n = 6$. (**B**) ORO staining was quantified and normalized to baseline staining. ***$P < 0.001$. $n = 6$. (**C**) Expression of adipogenic genes in WT and *GSNOR*$^{-/-}$ MSCs grown in adipogenic medium, analyzed by 1-way ANOVA (overall $P < 0.0001$). $n = 5$–7. *$P < 0.05$; ***$P < 0.001$, compared with WT, analyzed by Bonferroni's multiple comparison test. (**D**) Expression of *Cd36* in WT and *GSNOR*$^{-/-}$ MSCs grown in adipogenic medium. *$P < 0.05$. $n = 6$. (**E** and **F**) Expression of *Pparg* (**E**) (2-way ANOVA; for strain, $P = 0.0313$; for drug, $P = 0.5547$) and *Fabp4* (**F**) (2-way ANOVA; for strain, $P < 0.0001$; for drug, $P = 0.2736$) after GSNOR inhibitor treatment. *$P < 0.05$, compared with WT, analyzed by Bonferroni's multiple comparison test. $n = 3$. (**G**) ORO staining of WT and *GSNOR*$^{-/-}$ MSCs grown in adipogenic medium and treated with 50 μM or 100 μM GSNOR inhibitor (GSNORi) for 2 weeks. Scale bars: 100 μm. $n = 3$. (**H**) ORO staining was quantified (2-way ANOVA; for strain, $P < 0.0001$; for drug, $P = 0.0014$). **$P < 0.01$; ***$P < 0.001$, compared with WT, analyzed by Bonferroni's multiple comparison test. $n = 3$. Statistical significance between 2 groups was determined by unpaired Student's t test (2-tailed) and presented as mean ± SEM.

where NO forms S-nitrosothiols (SNOs) by binding to the cysteine thiols of proteins (14). S-nitrosoglutathione reductase (GSNOR), a denitrosylase, regulates S-nitrosylation through the degradation of S-nitrosoglutathione (GSNO), resulting in decreased protein SNOs. Impaired denitrosylation, as manifested in *GSNOR*$^{-/-}$ mice, alters multiple stem cell characteristics, including hematopoietic stem cell number and MSC endothelial differentiation (15, 16).

Here, we demonstrate that GSNOR-mediated PPARγ S-nitrosylation could be a pivotal, yet previously unrecognized, checkpoint regulator that balances MSC differentiation into adipocytes and osteoblasts. *GSNOR*$^{-/-}$ mice have decreased body weight and increased bone formation. MSCs isolated from *GSNOR*$^{-/-}$ mice exhibit decreased adipogenesis and enhanced osteogenesis, accompanied by decreased transcriptional activity of PPARγ attributed to increased PPARγ S-nitrosylation. Furthermore, we identified Cys 139 as the principle site of PPARγ inhibition by S-nitrosylation. This study identifies GSNOR-mediated denitrosylation as a mediator of MSC differentiation and body composition.

Results

GSNOR loss of function impairs adipogenesis of murine MSCs. MSCs were isolated and characterized as described previously (16) and were subjected to adipocyte differentiation conditions in vitro. *GSNOR*$^{-/-}$ cells grown in adipogenic medium had significantly less oil red O (ORO) staining, indicating a lower propensity to form fat droplets than WT cells (Figure 1, A and B). Expression of the adipogenic marker *Pparg* increased in both WT and *GSNOR*$^{-/-}$ cells following differentiation, but this increase was attenuated in *GSNOR*$^{-/-}$ cells (Figure 1C). Expression of multiple adipogenic transcription factors, such as CCAAT/enhancer-binding protein β (*Cebpb*), an upstream regulator of PPARγ, was decreased in *GSNOR*$^{-/-}$ MSCs (Figure 1C) as was expression of the downstream adipogenic effector of PPARγ fatty acid–binding protein 4 (*Fabp4*) (Figure 1C). CD36, a membrane-bound fatty acid translocase and downstream target of PPARγ, was also markedly decreased (87-fold) in *GSNOR*$^{-/-}$ MSCs (Figure 1D). Expression of adiponectin (*Adipoq*), another adipogenic marker, was unaffected (Supplemental Figure 1A; supplemental material available online with this article; doi:10.1172/JCI73780DS1).

To further probe the impact of GSNOR signaling, we incubated *GSNOR*$^{-/-}$ and WT MSCs with the GSNOR inhibitor 4-[[2-[[(2-cyanophenyl)methyl]thio]-4-oxothieno-[3,2d] pyrimidin-3(4H)-yl]methyl]-benzoic acid (50 μM and 100 μM) (17). *GSNOR*$^{-/-}$ cells were not affected by the inhibitor. In contrast, WT MSCs exhibited significantly decreased expression of *Pparg* and *Fabp4*, mimicking the knockout genotype (Figure 1, E and F). Furthermore, the GSNOR inhibitor decreased ORO staining in WT cells (Figure 1, G and H). Treatment with the NO donor GSNO (100 μM) inhibited fat-droplet formation in WT cells without affecting *Pparg* expression (Supplemental Figure 1, B–D). Surprisingly, fat-droplet formation in WT cells was also reduced after treating with the pan-NOS inhibitor Nω-nitro-L-arginine methyl ester hydrochloride (L-NAME, 30 μM) (Supplemental Figure 1, B–D), suggesting that a physiological level of NO is crucial for maintaining adipogenic capacity. Adipogenic differentiation of *GSNOR*$^{-/-}$ cells was not affected by treatment with 30 μM L-NAME (Supplemental Figure 1, B–D). Together, these results indicate that loss of GSNOR function inhibits adipogenic differentiation of MSCs.

GSNOR loss of function enhances osteogenic differentiation and MSC-mediated bone regeneration. We next examined the role of GSNOR in the osteogenic differentiation of MSCs. WT and *GSNOR*$^{-/-}$ MSCs were grown in osteogenic medium for 2 weeks, and Alizarin red-S (ALS) staining, indicative of calcium deposition, was quantified. *GSNOR*$^{-/-}$ cells produced significantly more calcium compared with WT cells (Figure 2A) and showed increased expression of the late osteogenic marker osteocalcin (*Bglap*) (Figure 2B). However, expression of the early osteogenic markers *Runx2* and osteopontin (*Spp1*) was not different between WT and *GSNOR*$^{-/-}$ cells at this time point (Supplemental Figure 2, A and B), likely due to osteogenic differentiation having already reached the late mineralization stage (Figure 2A and ref. 18). Therefore, we examined early osteogenic markers in MSCs prior to differentiation and found higher expression levels of *Runx2* (Figure 2C), *Spp1* (Figure 2D), and *Bglap* (Figure 2E) in *GSNOR*$^{-/-}$ cells compared with WT. Treatment of WT MSCs with the GSNOR inhibitor significantly increased osteogenic differentiation as measured by ALS staining and gene expression, while no effect was seen in *GSNOR*$^{-/-}$ cells (Figure 2, F–J). Osteogenic differentiation of *GSNOR*$^{-/-}$ MSCs was reduced by L-NAME, but osteogenic differentiation of WT cells was not affected by either L-NAME or GSNO (Supplemental Figure 2, C–E). Taken together, these results suggest that increased SNO bioavailability enhances the osteogenic potential of MSCs and that *GSNOR*$^{-/-}$ MSCs are more committed toward the osteoblast lineage.

Next, we assessed the impact of GSNOR on MSC differentiation in vivo and compared the in vivo bone regeneration capacity of WT and *GSNOR*$^{-/-}$ MSCs following subcutaneous implantation of cells within a GelFoam plug (ref. 19 and Figure 2K). After 7 weeks, MSC-mediated bone formation was significantly greater in *GSNOR*$^{-/-}$ cell implants (Figure 2, L and M). These data demonstrate that the enhanced osteogenic differentiation capacity of *GSNOR*$^{-/-}$ MSCs directly causes higher bone regeneration in vivo.

GSNOR$^{-/-}$ *mice have reduced body weight and bone mass*. We further sought to address the impact of altered MSC differentiation of *GSNOR*$^{-/-}$ cells on the phenotype of intact animals. Two-month-old male *GSNOR*$^{-/-}$ mice were smaller and weighed less than corresponding WT mice (Figure 3, A and B). *GSNOR*$^{-/-}$ mice had a lower percentage of fat mass (Figure 3C) and a higher percentage of lean mass, but lower lean mass weight (Figure 3D). Over the next 11 months, *GSNOR*$^{-/-}$ mice maintained this relatively lower body weight (Supplemental Figure 3A). Food intake was not altered in *GSNOR*$^{-/-}$ mice (Supplemental Figure 3B). We also measured adipocyte size, since weight gain is caused largely by adipocyte hypertrophy, a process that contributes to the enlargement of adipose tissue (20). *GSNOR*$^{-/-}$ epididymal adipocytes were, on average, significantly smaller than WT adipocytes (Figure 3E). In contrast to MSCs, expression of *Pparg* and its downstream target *Fabp4* were unchanged in *GSNOR*$^{-/-}$ white adipose tissue (WAT) (Figure 3F). Interestingly, expression of *Cebpd*, an upstream regulator of PPARγ, was increased in *GSNOR*$^{-/-}$ WAT, but that of *Cebpb* was not (Figure 3F). Together, these results show that intact *GSNOR*$^{-/-}$ animals have a phenotype consistent with impaired adipogenesis.

We next performed histological and μCT analyses of bone samples to assess bone formation and resorption in intact animals, testing the prediction that the *GSNOR*$^{-/-}$ mice exhibit increased bone formation. Analysis of calcein double labeling demonstrated a higher dynamic of bone formation rate (BFR) in *GSNOR*$^{-/-}$ mice relative to WT (Figure 4A). Consistent with these histological findings, parameters of bone formation and mineralization were increased in *GSNOR*$^{-/-}$ mice (Figure 4, B and C, and Supplemental Table 1), including osteoblast surfaces per bone surface (Ob.S/BS), mineralization apposition rate (MAR), and BFR/BS. Serum alkaline phosphatase, a bone formation marker, was not altered in *GSNOR*$^{-/-}$ mice (Supplemental Figure 3C).

Surprisingly and paradoxically, *GSNOR*$^{-/-}$ mice had lower overall bone mineral density (BMD) compared with WT mice (Figure 4D and Supplemental Figure 3D). μCT imaging of the vertebrae and femur demonstrated that the *GSNOR*$^{-/-}$ mice had reduced amounts of trabecular bone compared with WT mice (Figure 4, E and F). More specifically, *GSNOR*$^{-/-}$ mice had significantly less trabecular bone volume per total volume (BV/TV), trabecular thickness (Tb.Th), and trabecular number (Tb.N; Figure 4G). Trabecular separation (Tb.Sp), a measurement of average thickness

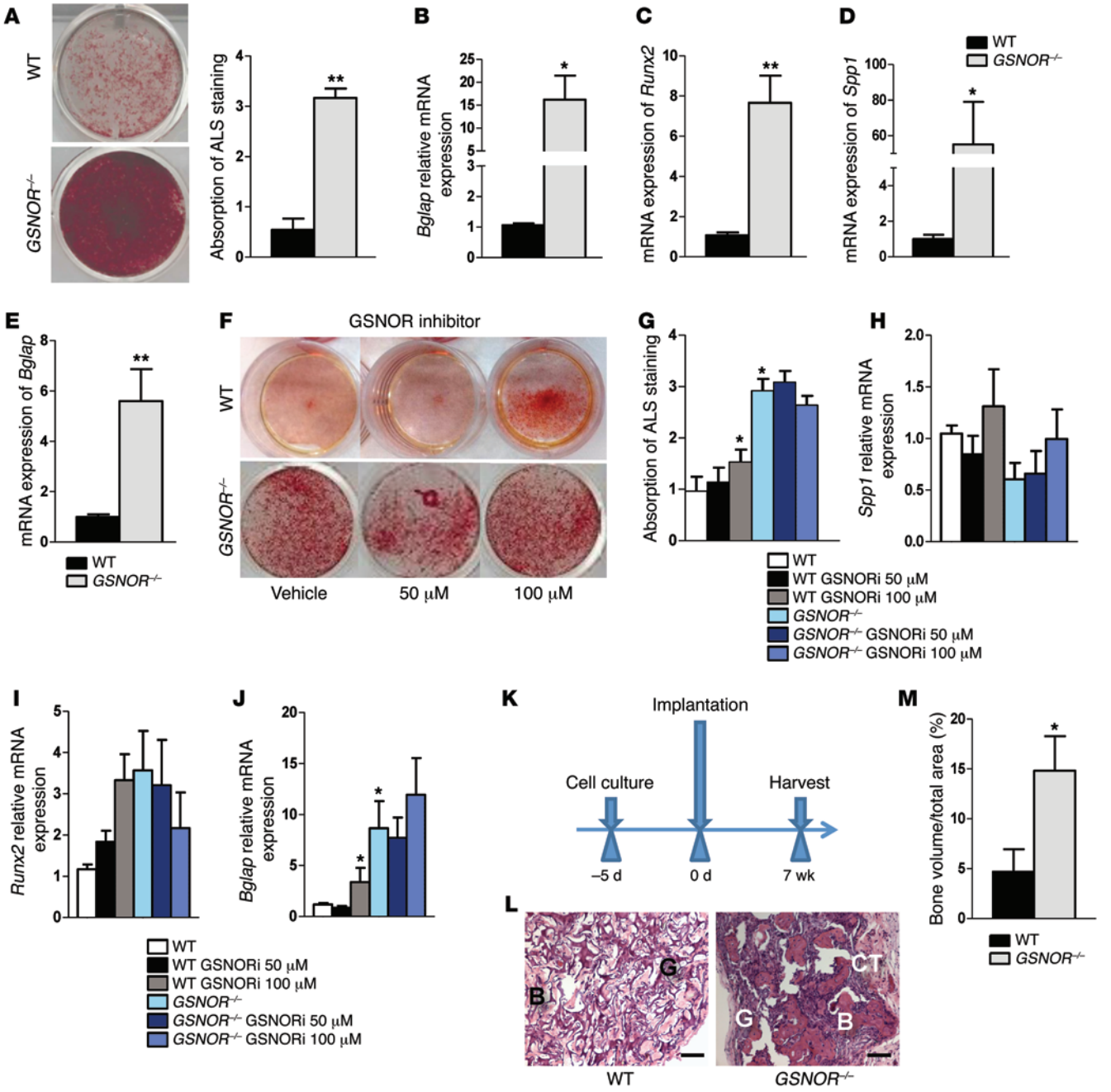

Figure 2. *GSNOR*$^{-/-}$ MSCs exhibit enhanced osteogenic differentiation. (**A**) Whole-well scan of ALS staining of WT and *GSNOR*$^{-/-}$ MSCs. ALS staining was quantified. $^{**}P < 0.01$. $n = 6$. (**B**) Expression of *Bglap* (osteocalcin) in MSCs grown in osteogenic medium. $^{*}P < 0.05$. $n = 6$. (**C**–**E**) Expression of *Runx2* (**C**), *Spp1* (osteopontin, **D**), and *Bglap* (osteocalcin, **E**) at baseline in the absence of osteogenic supplements. $^{*}P < 0.05$; $^{**}P < 0.01$. $n = 6$. (**F** and **G**) WT and *GSNOR*$^{-/-}$ MSCs were grown in osteogenic medium and treated with 50 μM or 100 μM GSNOR inhibitor for 2 weeks. ALS staining was performed and quantified (2-way ANOVA; for strain, $P = 0.0004$; for drug, $P = 0.9081$). $^{*}P < 0.05$, compared with WT, analyzed by Bonferroni's multiple comparison test or 1-way ANOVA within strain. $n = 3$. (**H**–**J**) Cells were treated similarly to those shown in **F** and **G**, and expression of *Spp1* (**H**), *Runx2* (**I**), and *Bglap* (**J**) was determined (2-way ANOVA; for strain, $P < 0.0001$; for drug, $P = 0.2829$). $^{*}P < 0.05$, compared with WT, analyzed by Bonferroni's multiple comparison test or 1-way ANOVA within strain. $n = 3$. (**K**) Scheme for assessing MSC-based bone regeneration in vivo. (**L**) H&E staining of tissue samples from NOD-SCID mice after subcutaneous implantation with WT or *GSNOR*$^{-/-}$ MSCs following the protocol described in **K**. H&E staining was quantified (**M**). Formation of bone (B) and connective tissue (CT) around GelFoam (G) are indicated. Scale bars: 500 μm. $n = 3$. (**M**) Semiquantitative analysis of new bone formation. $n = 3$. $^{*}P < 0.05$. Statistical significance between 2 groups was determined by unpaired Student's *t* test (2-tailed) and presented as mean ± SEM.

of the marrow cavities, was higher in *GSNOR*$^{-/-}$ mice (Figure 4H). Toluidine blue staining showed that *GSNOR*$^{-/-}$ mice had lower trabecular bone mass (Figure 4I). BMD of cortical bone was also significantly reduced (Supplemental Table 2).

Bone histomorphometric analysis of the femur indicated that *GSNOR*$^{-/-}$ mice had significantly increased osteoclast surfaces (Oc.S/BS) and eroded surfaces (ES/BS), indicative of increased bone resorption (Figure 4J and Supplemental Table 1). The

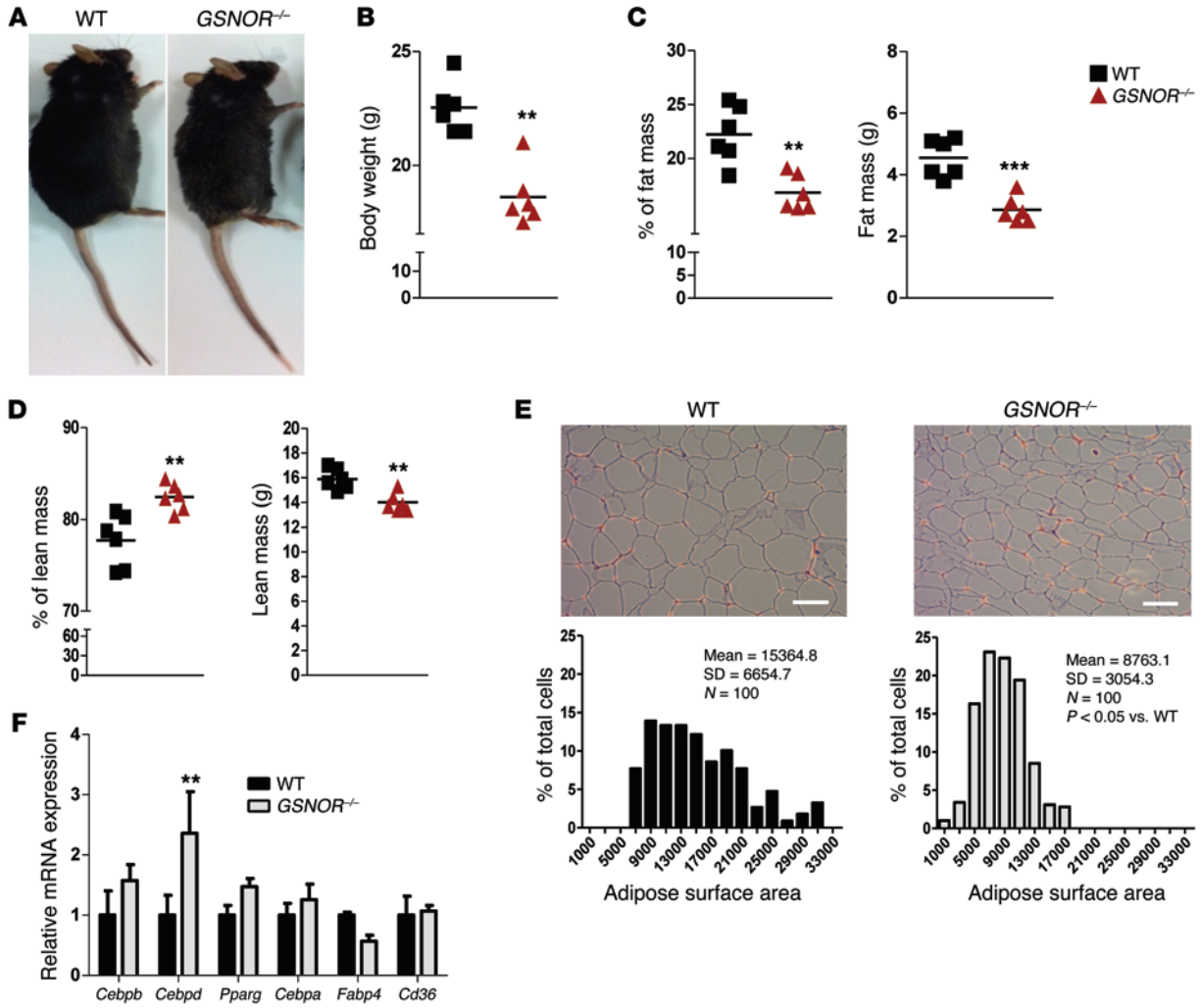

Figure 3. *GSNOR*$^{-/-}$ mice have reduced body weight, fat mass, and adipocyte size. (**A** and **B**) Whole-body morphology and body weight of 2-month-old male WT and *GSNOR*$^{-/-}$ mice. $^{**}P < 0.01$. $n = 6$. (**C** and **D**) Percentage and weight of fat mass (**C**) and percentage and weight of lean mass (**D**) of 2-month-old male mice were measured by DEXA. $^{**}P < 0.01$; $^{***}P < 0.001$. $n = 6$. (**E**) Adipose tissue was stained with H&E, and adipocyte surface area was quantified. Scale bars: 100 μm. $n = 3$. (**F**) Adipogenic gene expression in WAT (WT, $n = 5$; *GSNOR*$^{-/-}$, $n = 4$). Statistical significance was determined by 2-way ANOVA and presented as mean ± SEM. $^{**}P < 0.01$, compared with WT, analyzed by Bonferroni's multiple comparison test. Statistical significance between 2 groups was determined by unpaired Student's *t* test (2-tailed) and presented as mean ± SEM.

increased rate of bone formation and bone resorption seen in *GSNOR*$^{-/-}$ mice indicated higher bone turnover, with a net result of lower bone volume and reduced BMD.

To evaluate whether morphological phenotypes of the femur in *GSNOR*$^{-/-}$ mice actually caused mechanical fragility, we performed a 3-point bending test. In *GSNOR*$^{-/-}$ mice, maximum load and stiffness were both decreased (Figure 4, K and L), indicating mechanical weakness in the femur of *GSNOR*$^{-/-}$ mice. In addition, Young's module and resiliency were lower in *GSNOR*$^{-/-}$ mice (Figure 4, M and N).

GSNOR$^{-/-}$ *bone marrow mononuclear cells exhibit enhanced osteoclastogenesis*. To address the paradoxical findings of overall BMD in the context of increased osteoblast formation, we assessed the impact of GSNOR deficiency on osteoclasts. First, we verified our findings of increased bone resorption by measuring osteoclast number per bone perimeter (N.OC/B.Pm) in *GSNOR*$^{-/-}$ mice (Supplemental Table 1). We obtained bone marrow mononuclear cells (BMMNCs) from WT and *GSNOR*$^{-/-}$ mice and grew them in osteoclast differentiation medium for 6 days. Osteoclast differentiation was characterized by the presence of tartrate-resistant acid phosphatase–positive (TRAP-positive) cells containing more than 3 nuclei. The number of TRAP-positive osteoclasts was significantly increased in cultures of *GSNOR*$^{-/-}$ compared with WT BMMNCs (Supplemental Figure 4, A and B), suggesting that GSNOR loss of function promotes osteoclastogenesis. This result is consistent with the enhanced bone resorption phenotype observed in *GSNOR*$^{-/-}$ mice.

Altered calcium and phosphate homeostasis in GSNOR$^{-/-}$ *mice*. To gain additional insights into the paradoxical phenotype of enhanced bone resorption in the face of increased bone formation, we assessed calcium and phosphate homeostasis in the *GSNOR*$^{-/-}$ mice, as extracellular calcium and phosphate are required for matrix mineralization and the maintenance of normal bone structure. *GSNOR*$^{-/-}$ mice have lower BMD and a higher

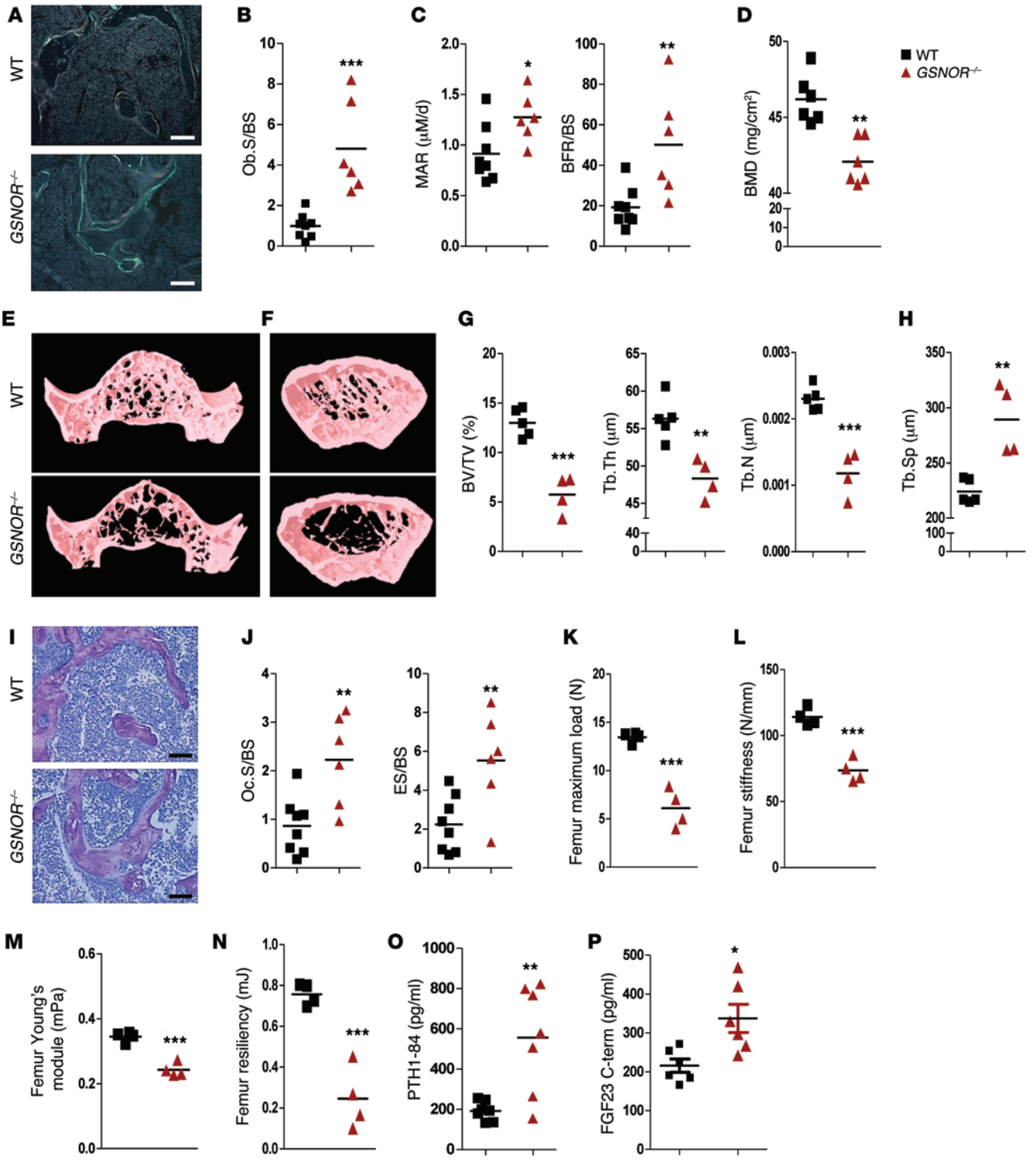

Figure 4. *GSNOR*$^{-/-}$ mice have enhanced bone formation and resorption. All studies were conducted in 2-month-old male WT and *GSNOR*$^{-/-}$ mice. (**A**) Calcein double labeling of the distal femur; mineralization front was stained in green. Scale bars: 200 μm. $n = 3$. (**B** and **C**) Quantification of histomorphometric analysis of Ob.S/BS (**B**) and MAR and BFR/BS (**C**) in the femur (WT, $n = 8$; *GSNOR*$^{-/-}$, $n = 6$). (**D**) Whole-body BMD. $n = 6$. (**E** and **F**) Representative images of the vertebra (**E**) and femur (**F**). $n = 3$. (**G** and **H**) Quantification of μCT analysis of BV/TV, Tb.Th, Tb.N (**G**), and Tb.Sp (**H**) (WT, $n = 5$; *GSNOR*$^{-/-}$, $n = 4$). (**I**) Toluidine blue staining of the distal femur, the mineralized bone was stained red. Scale bars: 200 μm. $n = 3$. (**J**) Quantification of histomorphometric analysis of osteoclast content in the femur (WT, $n = 8$; *GSNOR*$^{-/-}$, $n = 6$). (**K**–**N**) Femur maximum load (**K**), stiffness (**L**), Young's module (**M**), and resiliency (**N**). $n = 4$. (**O**) PTH level in the serum. $n = 7$. (**P**) Serum FGF23 level. C-term, C-terminus. $n = 6$. * $P < 0.05$; ** $P < 0.01$; *** $P < 0.001$. Statistical significance between 2 groups was determined by unpaired Student's t test (2-tailed) and presented as mean ± SEM.

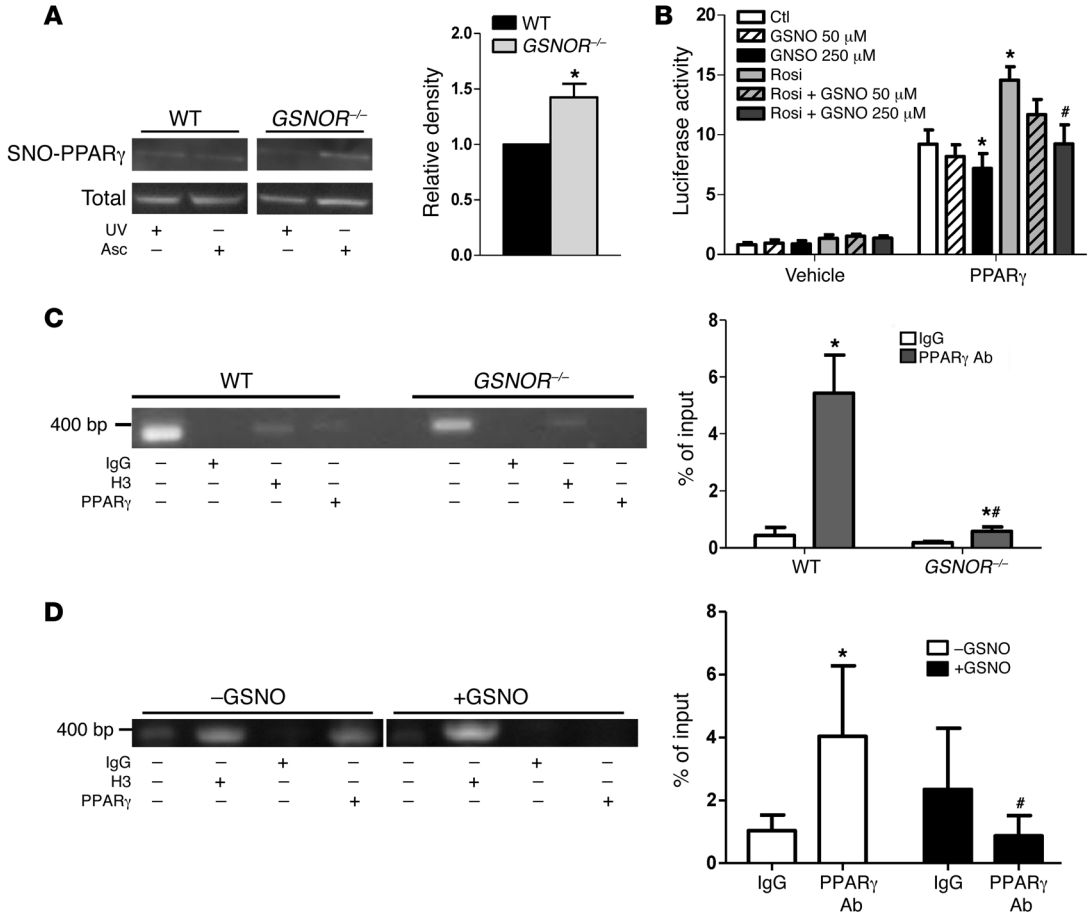

Figure 5. *GSNOR*$^{-/-}$ MSCs have enhanced constitutive S-nitrosylation of PPARγ with decreased transcriptional activity. (**A**) SNO-PPARγ in MSCs of WT versus *GSNOR*$^{-/-}$ mice was measured by SNO-RAC assay. UV, UV light; Asc, ascorbic acid. Pretreatment with UV light and omission of ascorbic acid were used as negative controls. *$P < 0.05$. $n = 3$. Statistical significance between 2 groups was determined by Student's t test. Representative blots show S-nitrosylated and total PPARγ. The relative ratio of S-nitrosylated PPARγ to total PPARγ in WT mice is arbitrarily defined as 1. The lanes were run on the same gel, but were noncontiguous. (**B**) PPARγ luciferase activity in HEK-293T cells treated with GSNO in the presence or absence of rosiglitazone (Rosi) (1 μM). 2-way ANOVA, *$P < 0.05$, compared with PPARγ CTL; #$P < 0.05$, compared with PPARγ rosiglitazone, analyzed by Bonferroni's multiple comparison test. $n = 5$. (**C**) ChIP analysis of PPARγ binding for the promoter region of FABP4 in WT and *GSNOR*$^{-/-}$ MSCs. *$P < 0.05$, compared with corresponding IgG; #$P < 0.05$, compared with WT PPARγ Ab group, analyzed by 2-way ANOVA Bonferroni's multiple comparison test. $n = 4$. (**D**) ChIP analysis of PPARγ binding to the promoter region of the *Fabp4* gene in WT MSCs treated with 500 μM GSNO. The lanes were run on the same gel, but were noncontiguous. *$P < 0.05$, compared with IgG without GSNO treatment; #$P < 0.05$, compared with PPARγ Ab without GSNO treatment, analyzed by Bonferroni's multiple comparison test (2-way ANOVA). $n = 4$. Data are presented as mean ± SEM.

mineralization rate (Figure 4, C and D). We first examined levels of parathyroid hormone (PTH), a key regulator of calcium and phosphate efflux from bone; indeed, PTH levels were higher in *GSNOR*$^{-/-}$ mice (Figure 4O). Despite this, both total and ionized calcium serum levels were not altered in *GSNOR*$^{-/-}$ mice (Supplemental Figure 5, A and B). While serum phosphate levels were equivalent in *GSNOR*$^{-/-}$ and WT mice (Supplemental Figure 5C), the urinary phosphate/creatinine ratio was higher in *GSNOR*$^{-/-}$ mice (Supplemental Figure 5D), consistent with elevated PTH levels. Paradoxically, *GSNOR*$^{-/-}$ mice also had an increased urine calcium/creatinine ratio (Supplemental Figure 5E), counter to the expected effect of elevated PTH. FGF23, a phosphaturic hormone secreted by osteocytes to enhance urinary calcium reabsorption (21, 22), was also increased in *GSNOR*$^{-/-}$ mice (Figure 4P). We attributed the increased urine calcium/creatinine ratio to the indirect effects of FGF23 to inhibit PTH. Thus, elevations of urinary calcium and phosphate excretion have the potential to contribute to the low bone mass phenotype of *GSNOR*$^{-/-}$ mice.

To test the association of the changes in calcium and phosphate metabolism to alterations in PPARγ in the *GSNOR*$^{-/-}$ mice, we treated mice with the PPARγ agonist rosiglitazone. While 1 week of rosiglitazone treatment did not alter the serum total calcium, ionized calcium, serum phosphate levels, or urinary calcium/creatinine ratio (Supplemental Figure 5, A–C, and E) in either mouse strain, rosiglitazone did increase the urinary phosphate/creatinine ratio in WT but not in *GSNOR*$^{-/-}$ mice (Supplemental Figure 5D). Importantly, rosiglitazone reduced elevated PTH levels toward normal, yet further increased FGF23 levels in the *GSNOR*$^{-/-}$ mice (Supplemental Figure 5, F and G). Additional experiments to measure PTH in fasting mice revealed similar findings. Our results suggest that GSNOR deficiency alters the balance of PTH-FGF23 crosstalk, contributing to the high bone turnover and bone loss.

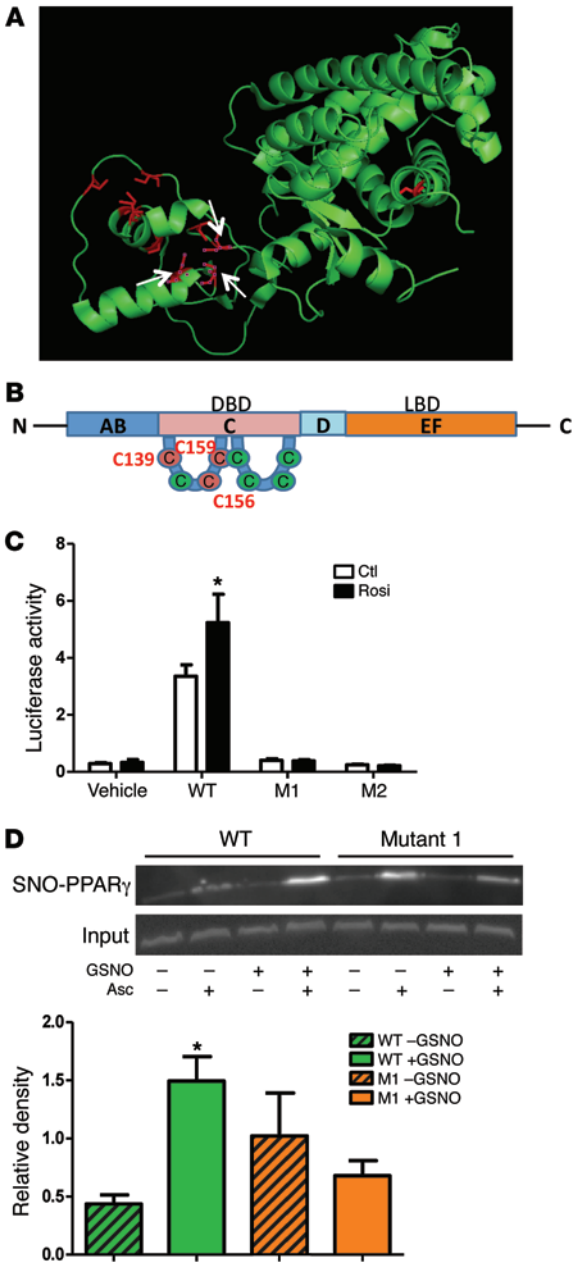

Figure 6. Identification of Cys 139 as a site of PPARγ S-nitrosylation. (**A**) A 3D structure of PPARγ showed the 10 cysteines in red, with white arrows labeling the 3 mutated ones. The 3D structure was derived from ref. 50. (**B**) A topology map of PPARγ with 3 mutated cysteines in red. DBD, DNA-binding domain; LBD, ligand-binding domain. (**C**) PPARγ luciferase activity in HEK-293T cells overexpressed with WT and mutants, in the presence or absence of the PPARγ agonist rosiglitazone (1 μM). *$P < 0.05$, compared with WT CTL, analyzed by Bonferroni's multiple comparison test (2-way ANOVA). $n = 4$. (**D**) SNO-PPARγ in HEK-293T cells overexpressed with WT and mutant 1 (Cys 139), measured by SNO-RAC. Omission of ascorbic acid was used as a negative control. *$P < 0.05$, compared with WT without GSNO treatment, analyzed by Bonferroni's multiple comparison test (2-way ANOVA). $n = 3$. Data are presented as mean ± SEM.

Constitutive PPARγ S-nitrosylation is increased in GSNOR$^{-/-}$ MSCs. We next evaluated the potential mechanism of impaired adipogenesis and enhanced osteogenesis seen in *GSNOR*$^{-/-}$ MSCs. PPARγ is a transcriptional master regulator of adipogenic differentiation and stimulates adipogenesis while inhibiting osteogenesis (23). We hypothesized that GSNOR loss of function increased PPARγ S-nitrosylation and decreased PPARγ function under basal conditions similarly to what occurs when PPARγ is S-nitrosylated in murine mesangial cells (24), consistent with PPARγ being a regulator of adipogenesis and osteogenesis. To test this hypothesis, we performed SNO resin-assisted capture (SNO-RAC) assays on undifferentiated MSCs from WT and *GSNOR*$^{-/-}$ mice (25). S-nitrosylated proteins were captured by thiol-reactive resin, and PPARγ S-nitrosylation status was assessed by immunoblotting. Although, as previously mentioned, *Pparg* mRNA expression from *GSNOR*$^{-/-}$ MSCs was higher following adipogenic differentiation (Figure 1C), there was no difference in the protein expression of PPARγ in undifferentiated MSCs (Figure 5A, total input lane). Importantly, *GSNOR*$^{-/-}$ MSCs demonstrated approximately 50% greater S-nitrosylation compared with WT cells under basal conditions (Figure 5A, upper lane; the relative density ratio of S-nitrosylated PPARγ/total PPARγ in *GSNOR*$^{-/-}$ mice was 1.57-fold ± 0.33-fold compared with WT mice). The identification of endogenous SNO in the SNO-RAC assay was validated by the elimination of signals by UV irradiation applied prior to the assay (which cleaves the SNO bond) and the omission of ascorbate, which prevents SNOs from being reduced (26). These data demonstrate increased S-nitrosylation of PPARγ as a potential mechanism for the decreased adipogenesis and enhanced osteogenesis of *GSNOR*$^{-/-}$ MSCs.

S-nitrosylated PPARγ has decreased transcriptional activity. To determine whether enhanced S-nitrosylation of PPARγ affects its transcriptional activity, we used a luciferase reporter assay. 293T cells were cotransfected with firefly luciferase under the control of a PPARγ response element (PPRE) (27) plus either a plasmid-encoding PPARγ or the empty vector control. Cells were treated with vehicle or the NO donor GSNO for 5 hours (50 or 250 μM). GSNO treatment resulted in an increase of PPARγ S-nitrosylation without affecting PPARγ protein expression (Supplemental Figure 6) and also significantly decreased PPARγ luciferase activity (Figure 5B). These results suggest that PPARγ transcriptional activity is decreased upon GSNO-induced S-nitrosylation. Interestingly, GSNO-induced downregulation of PPARγ transcriptional activity was not rescued by rosiglitazone (Figure 5B), suggesting a ligand-independent mechanism.

GSNOR$^{-/-}$ MSCs exhibited decreased expression of *Fabp4* compared with WT MSCs following adipogenic differentiation (Figure 1C). PPARγ is found in the cytoplasm, but nuclear translocation of PPARγ is crucial for its function (28). No difference in PPARγ nuclear localization was observed in WT and *GSNOR*$^{-/-}$ MSCs (Supplemental Figure 7). To assess whether S-nitrosylation of PPARγ affects transcription of its target gene, *Fabp4*, we performed ChIP assays. Histone 3 (H3) Ab–treated samples acted as positive controls. At baseline, the binding affinity of PPARγ for the promoter region of *Fabp4* was decreased in *GSNOR*$^{-/-}$ MSCs (Figure 5C). Furthermore, WT MSCs treated with 500 μM GSNO for 5 hours were found to have decreased PPARγ-binding affinity for the *Fabp4* promoter region compared with vehicle-treated cells (Figure 5D). This decrease in PPARγ-binding affinity was accom-

panied by an increase in PPARγ S-nitrosylation without altering its expression (Supplemental Figure 8). These data are consistent with the decreased adipogenesis seen in WT cells treated with GSNO and suggest that S-nitrosylated PPARγ has decreased affinity for the promoter of FABP4. Together, our results suggest that increased protein S-nitrosylation due to a lack of GSNOR reduces the transcriptional activity of PPARγ.

Identification of Cys 139 as a site of PPARγ S-nitrosylation. To determine which cysteines are S-nitrosylation targets, we generated 2 cysteine-to-alanine mutations by site-directed mutagenesis: Cys 139 single mutation and Cys 156/159 double mutation (Supplemental Figure 9). PPARγ has 10 cysteines, and a 3D structure of PPARγ shows the 10 cysteines in red, with white arrows indicating the 3 mutated residues (Figure 6A). A topology map of PPARγ indicated that the 3 mutated cysteines are located within the first zinc-finger structure of the regulatory domain (Figure 6B). Cys 139 was identified by GPS-SNO 1.0 software and conforms to an acid-base nitrosylation conservative motif (14, 29). The Cys 156/159 double mutation was first characterized by the Spiegelman group, who found that this mutation could cause diminished adipogenesis in preadipocytes (30). We first characterized the cellular localization of these mutants in HEK-293T cells to determine whether cysteine mutations lead to a disruption of protein 3D structure. All the mutants localized primarily to the nucleus of the cells in a pattern similar to that of WT PPARγ protein (Supplemental Figure 10). Furthermore, the luciferase activity of the 2 PPARγ mutants was diminished and could not be rescued by rosiglitazone, possibly due to a disruption of the zinc-finger structure (Figure 6C). We overexpressed WT and mutant PPARγ in HEK-293T cells. Cells were exposed to vehicle or GSNO, and PPARγ S-nitrosylation was measured by SNO-RAC. Mutation of Cys 139 to alanine eliminated the robust S-nitrosylation induced by GSNO (Figure 6D). However, the double PPARγ mutation (Cys 156 and 159) exhibited an S-nitrosylation response to GSNO similar to that of WT PPARγ (Supplemental Figure 11). These data suggest what may be a novel mechanism of PPARγ transcriptional regulation: S-nitrosylation of cysteine 139 induced alteration of the zinc-finger motif. Our data suggest that the decreased PPARγ transcriptional activity seen in *GSNOR*$^{-/-}$ MSCs can be attributed to higher levels of PPARγ S-nitrosylation, leading to the disruption of the first zinc-finger structure.

Discussion

Bone marrow–derived MSCs are a common precursor to adipocytes and osteoblasts (31). Although lineage-fate specification is controlled by crosstalk between multiple key transcription factors, higher order regulation of this process remains poorly understood. While PPARγ (7) and NO signaling participate in fate decisions between bone and fat lineages, the interaction between these control mechanisms has not yet been established. Here, we used MSCs derived from mice deficient in the prototypic denitrosylase GSNOR to show that excessive S-nitrosylation of PPARγ contributes to diminished adipogenic and increased osteoblastic differentiation. This phenotype is associated with decreased PPARγ transcriptional activity, as illustrated by diminished binding to *Fabp4*. We further identified S-nitrosylation of Cys 139 as a principle mechanism of PPARγ transcriptional inhibition. Together, these findings offer insights into the regulation of cell fate decisions in adult mesenchymal tissue homeostasis and provide potential therapeutic strategies to offset disorders of bone loss.

NO regulates adipocyte and osteoblast differentiation (32, 33); all 3 NOS isoforms are expressed in osteoblasts, and all except NOS1 are expressed in adipocytes (34, 35). With regard to downstream effects, NO has a biphasic effect on bone, where low concentrations of NO produced by NOS3 are essential for bone formation, while high concentrations of NO produced by NOS2 are inhibitory (36, 37). While WT and *GSNOR*$^{-/-}$ MSCs constitutively express NOS1 and NOS2, but not NOS3, *GSNOR*$^{-/-}$ MSCs have elevated NOS1 expression (16). The use of mice with a targeted deletion of GSNOR circumvents the disparities caused by varied NOS expression in MSCs and allows us to define the role of S-nitrosylation in NO-regulated adipocyte and osteoblast differentiation.

PPARγ regulates adipogenesis and osteogenesis by multiple posttranslational modifications, including phosphorylation, ubiquitination, and SUMOylation (38). Here, we show that the posttranslational modification S-nitrosylation participates fundamentally in PPARγ transcriptional activity. PPARγ regulates transcription via PPRE-dependent and -independent mechanisms. However, the transcriptional regulation of PPARγ in MSCs has heretofore been unknown. Our results reveal that S-nitrosylation of PPARγ inhibits its transcriptional activity at the *Fabp4* promoter in MSCs. Our findings in *GSNOR*$^{-/-}$ MSCs fully recapitulate the differentiation phenotypes of bone marrow cells from mice with *Pparg* haploinsufficiency (7), providing further confirmation that S-nitrosylation inhibits PPARγ activity. Lower expression of CEBPβ observed in *GSNOR*$^{-/-}$ MSCs indicates that events upstream of PPARγ were altered, providing an additional mechanism for decreased adipogenesis.

Our data indicated that Cys 139 of PPARγ is a primary S-nitrosylation target of exogenously supplied SNO. The amino acids surrounding Cys 139 conform to an acid-base motif previously described as a conservative S-nitrosylation domain (14), while the locations of Cys 156 and Cys 159 do not conform to this motif. The acid-base motif structure provides the thiolate anion with a more ionizable environment, thus making the cysteine more accessible to SNOs due to cysteine stabilization (39). The acid-base structure can either be adjacent to the cysteine in primary sequence or in proximity due to the 3D structure. In the PPARγ primary sequence, Cys 139 is flanked by glutamic acid and arginine. Our finding of Cys 139, but not Cys 156 and 159, as a PPARγ S-nitrosylation target provides additional evidence of the existence of a conservative S-nitrosylation motif.

The mechanism of PPARγ- and NO-signaling interaction is not well established. PPARγ stimulates NO production by enhancing NOS3 expression (40). PPARγ can also increase NOS2 activity and modulate immune reaction (41). Here, we provide what we believe to be a novel feedback regulation of PPARγ transcriptional activity by NO-mediated S-nitrosylation. NO is an important regulator of zinc-finger transcription factors (42, 43). SNOs inhibit the DNA-binding activity of the zinc-finger transcription factors, such as EGR-1 and SP1 (39). It has been proposed that this inhibition is due to the S-nitrosylation of a thiolate group within the zinc fin-

ger. This posttranslational modification changes the coordination of zinc ion with cysteines, thus disrupting the zinc-finger structure (39). Our data provide further support to this theory, suggesting that in *GSNOR*$^{-/-}$ MSCs, a higher level of PPARγ S-nitrosylation leads to disruption of the first zinc-finger structure and decreased PPARγ transcriptional activity.

Our studies also reveal a complex phenotype with regard to osteoblast differentiation of MSCs. Here, we showed that osteogenic differentiation was augmented in *GSNOR*$^{-/-}$ MSCs, and this finding was confirmed by experiments with the GSNOR inhibitor. In the intact animal, however, while there is evidence of increased bone formation, this effect is offset by augmented bone resorption due to enhanced formation of osteoclasts that arise from BMMNCs. Thus S-nitrosylation signaling participates in the formation of both osteoblasts and osteoclasts.

We further performed a detailed analysis of calcium/phosphate metabolism to gain additional insights into the skeletal phenotype of GSNOR-deficient animals (Supplemental Figure 12). *GSNOR*$^{-/-}$ mice had higher serum levels of PTH and FGF23 and increased urinary loss of phosphate and calcium, which together can contribute to diminished bone density. Chronic PTH exposure increases osteoclast activity and bone resorption (44). Ongoing studies are underway to establish the relative contributions of altered hormonal homeostasis and increased PPARγ S-nitrosylation to stem cell differentiation and the pathological bone loss phenotypes.

GSNOR$^{-/-}$ mice also represent an interesting model of hormonal regulation. The elevated PTH levels, accompanied by high bone turnover and upregulated FGF23, partly resemble secondary hyperparathyroidism. The elevated FGF23 and concurrent upregulation of PTH represent the impaired calcium-induced inhibition of PTH in chronic kidney diseases (45). Rosiglitazone treatment simultaneously increased FGF23 levels while reducing PTH in *GSNOR*$^{-/-}$ mice, but without significantly reducing urinary calcium. The differential response to rosiglitazone suggests that GSNOR loss of function alters the set point for FGF23, PTH, and calcium phosphate sensing in multiple organs, including parathyroid gland and kidney. Importantly, PPARγ agonists are known to upregulate α-klotho, a necessary coreceptor of FGF23 (46). However, the absence of hypocalcemia suggests a chronic compensation effect of high PTH or normocalcemic primary hyperparathyroidism. Further study is needed to elucidate the role of GSNOR in parathyroid function and calcium homeostasis.

In summary, our data reveal that GSNOR modulates PPARγ S-nitrosylation without affecting overall abundance of this transcription factor. Nitrosylated PPARγ has diminished transcriptional activity, which is associated with reduced adipocyte differentiation and increased osteoblast formation. Thus, S-nitrosylation participates in lineage bifurcation between adipocytes and osteoblasts. These findings have important implications and offer broad insights for understanding the regulation of lineage specification of adult precursor cells. Our results also suggest that GSNOR may contribute to PTH regulation and calcium urinary excretion, which in turn can affect the phenotype of GSNOR$^{-/-}$ mice. Together, these findings may provide mechanistic support for therapeutic strategies designed to offset disorders characterized by pathologic bone loss and/or excessive adipogenesis.

Methods

Mice. *GSNOR*$^{-/-}$ mice were generated as previously described (47). WT C57BL/6J mice were purchased from the Jackson Laboratories. Two-month-old male mice were used in this study. Mice were fed standard normal chow containing 4% fat ad libitum unless stated otherwise. For the rosiglitazone study, mice were fed with rosiglitazone mixed chow (Harlan, 150 mg rosiglitazone/kg chow) for 1 week.

Bone analyses. Fat mass, lean mass, and BMD were measured by dual-energy x-ray absorptiometry (DEXA). μCT was done as described (48). Quantitative histomorphometric analysis was conducted in a blinded fashion with the OsteoMeasure morphometry system (Osteometrics). To label mineralization deposition, sequential subcutaneous injections of 12 mg/ml calcein (Sigma-Aldrich; 20 mg/kg body weight) and 6 mg/ml demeclocycline (Sigma-Aldrich; 15 mg/kg body weight) in 2% sodium bicarbonate solution were performed. Calcein and demeclocycline were injected 9 days and 2 days, respectively, before the mice were euthanized. Static parameters of bone formation and resorption were measured in a defined area between 181 μm and 725 μm from the growth plate. For dynamic histomorphometry, mineralizing surface per bone surface and mineral apposition rate were measured in unstained sections under ultraviolet light, using a B-2A set long-pass filter consisting of an excitation filter ranging from 450 to 490 nm, a barrier filter at 515 nm, and a dichroic mirror at 500 nm. BFR was calculated. The terminology and units used are those recommended by the Histomorphometry Nomenclature Committee of the American Society for Bone and Mineral Research.

Plasma and urine parameters. 24-hour urine was collected from individual mice housed in a metabolic chamber (Tecniplast). Serum was collected from these mice by cardiac puncture followed by centrifugation of the blood at 1500 *g* for 20 minutes. Concentrations of plasma and urinary inorganic calcium and phosphate were determined by Vitros Dry Slide Chemistry Analyzer (Ortho-Clinical Diagnostics Inc.). Ionized calcium was measured using VetScan i-STAT 1 handheld analyzer (Abaxis Inc.). Concentration of urine creatinine was determined by Vitros Dry Slide Chemistry Analyzer. Plasma FGF23 concentrations were measured using the FGF-23 ELISA Kit (Immutopics Inc.). Plasma PTH concentrations were measured using the PTH ELISA kit (Immutopics Inc.).

Three-point bending test. The left femurs and tibias were tested in an Instron testing machine (Model 3344, Instron Corp.). Fresh-frozen bones were thawed to room temperature (22°C). For the femurs, the anterior cortex at the middiaphysis was placed in compression and the posterior cortex in tension during the test; for the tibias, the posterolateral cortex at the middiaphysis was placed in compression and the anteromedial cortex in tension. The lower support points were separated by an extent of 50% of the femoral length (femur length/2) and by 63% of the tibial length (tibia length/1.6). A constant displacement rate of 0.03 mm/s was applied until the bone fractured. Fracture was taken as complete loss of load-carrying ability. To stabilize the specimen, a small preload (5% of the average maximal load) was applied before actual testing. During the bending test, load-displacement data were collected by a computerized data-acquisition system at a sampling rate of 80 Hz. The biomechanical properties evaluated were the maximum load (a measure of the maximum force that the bone withstood before fracture [N]), resilience (a measure of the ability of a bone to suffer elastic deformity [J]), Young's modulus (mPa), and stiff-

ness (N/mm) (which are measures of the extrinsic rigidity of the bone tissue), and ductibility (a measure of the ability of bone to resist to the propagation of cracks).

Cells. All cells were maintained under a 37°C/5% CO_2 atmosphere. MSCs were harvested and characterized as described previously (16). MSCs were grown with 20% (vol/vol) FBS (Atlanta Biologicals), 1% (vol/vol) penicillin and streptomycin, and αMEM (Invitrogen). BMMNCs were maintained with 10% (vol/vol) FBS, 1% (vol/vol) penicillin and streptomycin, and αMEM (Invitrogen). HEK-293T cells were cultured with 10% (vol/vol) FBS, 1% (vol/vol) penicillin and streptomycin, and DMEM (Invitrogen).

Ex vivo bone marrow differentiation. MSCs generated from WT and *GSNOR*$^{-/-}$ mice were cultured for 14 days in adipogenic differentiation medium (containing 1 μM dexamethasone, 10 μg/ml insulin, 100 μM, indomethacin, and 0.5 μM 1-methyl-3-isobuthyxanthine) or osteogenic differentiation medium (containing 100 nM dexamethasone, 0.2 mM ascorbic acid, and 10 mM β-glycerophosphate). At the end of differentiation, fat-droplet formation in adipogenic differentiation was stained and quantified by ORO staining, and calcium formation in osteogenic differentiation was analyzed by ALS staining. Baseline staining served as negative control.

ORO and ALS quantification. ORO quantification was performed using ImageJ (49). Pictures first underwent "split channels" to generate a clear contrast. Then the contrast between positive and negative staining was adjusted evenly using "threshold." The percentages of positive staining areas were automatically produced by the "analyze particles" function. ALS quantification was conducted by absorbing the dye with 10% cetylpyridinium chloride buffered with 10 mM sodium phosphate (pH 7) and measuring absorption at 550 nm with a spectrophotometer.

In vivo osteogenic differentiation. Approximately 2.0 × 10^6 MSCs were loaded with GelFoam (5 mm × 5 mm × 5 mm; Pfizer) as a carrier and subcutaneously implanted into the dorsal surfaces of 2- to 4-month-old female NOD-SCID mice as described previously (19). At 7 weeks after implantation, the implants were harvested and H&E staining of the histological sections was analyzed using ImageJ.

RNA extraction and quantitative real-time PCR. MSC RNA was extracted using the RNeasy kit (QIAGEN) according to the manufacturer's instructions. RNA from WAT was extracted using the RNAeasy Lipid Tissue Mini Kit (QIAGEN). Gene expression was determined using TaqMan Gene Expression Assays. First-strand cDNA was prepared using a high-capacity cDNA reverse transcriptase kit (Applied Biosciences, Life Technologies). Reverse-transcribed cDNA was used for quantitative real-time PCR (RT-PCR) using predesigned TaqMan probes for mouse adipogenic markers (*Pparg*, adiponectin, *Fabp4*, *Cd36*, *Cebpa*, *Cebpb*, and *Cebpd*) and for osteogenic markers (*Runx2*, osteopontin, and osteocalcin) as well as the internal control *Gusb*. The actual number of transcripts was calculated by ΔCt. Fold changes were calculated by the ΔΔCt method using endogenous controls for normalization.

Western blot. For protein extraction, MSCs were homogenized in RIPA buffer with protease inhibitors. The cell lysates were centrifuged at 14,000 *g* for 15 minutes at 4°C, and the supernatant was boiled in 4× sample buffer and analyzed by SDS-PAGE (Invitrogen), as described in the manufacturer's protocol. For primary Ab against PPARγ (Santa Cruz Biotechnology Inc., clone H100), an HRP-conjugated secondary Ab (Promega) was used.

S-nitrosylation. SNO-RAC assay was performed in the dark as described (25). Briefly, MSCs were homogenized in HEN buffer (250 mM Hepes, 1 mM EDTA, and 0.1 mM neocuproine, pH 7.7). Free cysteine residues were blocked with MMTS and reacted with or without sodium ascorbate. Protein lysate was incubated with thiol-reactive resin (Sigma-Aldrich) for 5 hours. Resin-captured proteins were eluted using 50 μl elution buffer (20 mM HEPES, 100 mM NaCl, 1 mM EDTA, 100 mM β-mercaptoethanol) and heated at 95°C for 5 minutes in reducing SDS–PAGE loading buffer. The expression of PPARγ was determined by Western blot analysis.

ChIP assay. ChIP *Fabp4* promoter sequence was provided by F. Picard (Université Laval, Quebec, Canada). WT MSCs were treated with increasing concentrations of GSNO for 5 hours and then harvested for ChIP analysis, as previously described. Chromatin was immunoprecipitated with an anti-PPARγ Ab (Santa Cruz Biotechnology Inc., clone H100). RT-PCR amplification of the immunoenriched DNA samples was performed using primers for the *Fabp4* promoter (5′-ATGTCACAGGCATCTTATCCACC-3′ and 5′-AACCCTGCCAAAGAGACAGAGG-3′) and detected by agarose gel electrophoresis and RT-PCR.

Luciferase assay. The PPRE luciferase construct and PPARγ overexpression construct were obtained from Addgene (originally provided by B. Spiegelman, Harvard Medical School, Boston, Massachusetts, USA). Luciferase assay was performed according to the protocol of the Dual-Luciferase Reporter Assay System (Promega). The PPRE sequence was from the Spiegelman group: PPRE × 3 (5′-GTCGACAGGGGACCAGGACAAAGGTCACGTTCGGGAGTCGAC, 3 copies). Cells were lysed in 200 μl Passive Lysis Buffer (Promega). Duplicate 20 μl samples were mixed with 100 μl of Luciferase Assay Reagent (Promega). Luciferase activity was measured using a SIRIUS luminometer (Berthold Detection System, v3.1). Luminescence in each sample was normalized to Renilla luciferase activity.

Mutagenesis. Cysteine-to-serine mutations were constructed by GENEWIZ. HEK-293T cells were transfected with WT and mutant PPARγ by Lipofectamine 2000. 24 hours after transfection, cell lysates were collected and SNO-RAC was performed as described above. Cell lysates were treated with 100 μM GSNO for 10 minutes prior to SNO-RAC.

For further information and uncut gels, see Supplemental Experimental Procedures.

Statistics. Comparisons of 2 groups were performed using 2-tailed, unpaired Student's *t* test and presented as mean ± SEM. Means of more than 2 groups were compared by 1-way ANOVA or by 2-way ANOVA when 2 conditions were involved. Bonferroni's post hoc tests were applied when appropriate. $P < 0.05$ was considered significant.

Study approval. All protocols and experimental procedures with animals were approved by the Institutional Animal Care and Use Committee of the University of Miami.

Acknowledgments

This research was supported by NIH grant R01-HL094849 (to J.M. Hare) and American Heart Association grant 12PRE11340006 (to Y. Cao). J.M. Hare is also funded by NIH grants R01 HL110737-01, R01 HL107110, and R01HL084275 and a grant from the Starr Foundation. We thank Rosemeire Kanashiro-Takeuchi, Lauro Takeuchi, Claudia Rodrigues, Shathiyah Kulandavelu, Raul A.

Dulce, Ivonne H. Schulman, Christian Faul, Pamela Robey, Guoxin Ni, Gaofeng Wang, Aline Martin, and Carolyn Cray for help with techniques; Pereira Renata for bone histomorphometric analysis; and Carmen Perez for preparing the histologic sections.

Address correspondence to: Joshua M. Hare, Interdisciplinary Stem Cell Institute, Biomedical Research Building, Room 909, 1501 NW 10th Avenue, Miami, Florida 33136, USA. Phone: 305.243.5579; E-mail: jhare@med.miami.edu.

Samirah A. Gomes's present address is: Nephrology Division, University of São Paulo, São Paulo, Brazil.

Erika B. Rangel's present address is: Institute of Education and Research, Albert Einstein Hospital, São Paulo, Brazil.

Tatiana L. Fonseca and Antonio C. Bianco's present address is: Division of Endocrinology and Metabolism, Rush University Medical Center, Chicago, Illinois, USA.

1. Dominici M, et al. Minimal criteria for defining multipotent mesenchymal stromal cells. The International Society for Cellular Therapy position statement. *Cytotherapy*. 2006;8(4):315–317.
2. Caplan AI. Adult mesenchymal stem cells for tissue engineering versus regenerative medicine. *J Cell Physiol*. 2007;213(2):341–347.
3. Meunier P, Aaron J, Edouard C, Vignon G. Osteoporosis and the replacement of cell populations of the marrow by adipose tissue. A quantitative study of 84 iliac bone biopsies. *Clin Orthop Relat Res*. 1971;80:147–154.
4. Nishikawa K, et al. Maf promotes osteoblast differentiation in mice by mediating the age-related switch in mesenchymal cell differentiation. *J Clin Invest*. 2010;120(10):3455–3465.
5. McDonough AK, Rosenthal RS, Cao X, Saag KG. The effect of thiazolidinediones on BMD and osteoporosis. *Nat Clin Pract Endocrinol Metab*. 2008;4(9):507–513.
6. Kaplan FS, Shore EM. Progressive osseous heteroplasia. *J Bone Miner Res*. 2000;15(11):2084–2094.
7. Akune T, et al. PPARγ insufficiency enhances osteogenesis through osteoblast formation from bone marrow progenitors. *J Clin Invest*. 2004;113(6):846–855.
8. Tontonoz P, Hu E, Devine J, Beale EG, Spiegelman BM. PPARγ 2 regulates adipose expression of the phosphoenolpyruvate carboxykinase gene. *Mol Cell Biol*. 1995;15(1):351–357.
9. Hemmrich K, et al. Nitric oxide and downstream second messenger cGMP and cAMP enhance adipogenesis in primary human preadipocytes. *Cytotherapy*. 2010;12(4):547–553.
10. Hwang JH, et al. Idesolide inhibits the adipogenic differentiation of mesenchymal cells through the suppression of nitric oxide production. *Eur J Pharmacol*. 2012;685(1):218–223.
11. van't Hof RJ, Macphee J, Libouban H, Helfrich MH, Ralston SH. Regulation of bone mass and bone turnover by neuronal nitric oxide synthase. *Endocrinology*. 2004;145(11):5068–5074.
12. Hukkanen M, et al. Cytokine-stimulated expression of inducible nitric oxide synthase by mouse, rat, and human osteoblast-like cells and its functional role in osteoblast metabolic activity. *Endocrinology*. 1995;136(12):5445–5453.
13. Armour KE, et al. Defective bone formation and anabolic response to exogenous estrogen in mice with targeted disruption of endothelial nitric oxide synthase. *Endocrinology*. 2001;142(2):760–766.
14. Hess DT, Matsumoto A, Kim SO, Marshall HE, Stamler JS. Protein S-nitrosylation: purview and parameters. *Nat Rev Mol Cell Biol*. 2005;6(2):150–166.
15. Lima B, et al. Endogenous S-nitrosothiols protect against myocardial injury. *Proc Natl Acad Sci U S A*. 2009;106(15):6297–6302.
16. Gomes SA, et al. S-nitrosoglutathione reductase (GSNOR) enhances vasculogenesis by mesenchymal stem cells. *Proc Natl Acad Sci U S A*. 2013;110(8):2834–2839.
17. Sanghani PC, et al. Kinetic and cellular characterization of novel inhibitors of S-nitrosoglutathione reductase. *J Biol Chem*. 2009;284(36):24354–24362.
18. Kofron MD, Li X, Laurencin CT. Protein- and gene-based tissue engineering in bone repair. *Curr Opin Biotechnol*. 2004;15(5):399–405.
19. Bianco P, Kuznetsov SA, Riminucci M, Gehron RP. Postnatal skeletal stem cells. *Methods Enzymol*. 2006;419:117–148.
20. Li P, et al. Adipocyte NCoR knockout decreases PPARγ phosphorylation and enhances PPARγ activity and insulin sensitivity. *Cell*. 2011;147(4):815–826.
21. Quarles LD. Endocrine functions of bone in mineral metabolism regulation. *J Clin Invest*. 2008;118(12):3820–3828.
22. Andrukhova O, et al. FGF23 promotes renal calcium reabsorption through the TRPV5 channel. *EMBO J*. 2014;33(3):229–246.
23. Kawai M, Rosen CJ. PPARγ: a circadian transcription factor in adipogenesis and osteogenesis. *Nat Rev Endocrinol*. 2010;6(11):629–636.
24. Kuncewicz T, Sheta EA, Goldknopf IL, Kone BC. Proteomic analysis of S-nitrosylated proteins in mesangial cells. *Mol Cell Proteomics*. 2003;2(3):156–163.
25. Forrester MT, Thompson JW, Foster MW, Nogueira L, Moseley MA, Stamler JS. Proteomic analysis of S-nitrosylation and denitrosylation by resin-assisted capture. *Nat Biotechnol*. 2009;27(6):557–559.
26. Forrester MT, Foster MW, Benhar M, Stamler JS. Detection of protein S-nitrosylation with the biotin-switch technique. *Free Radic Biol Med*. 2009;46(2):119–126.
27. Kim JB, Wright HM, Wright M, Spiegelman BM. ADD1/SREBP1 activates PPARγ through the production of endogenous ligand. *Proc Natl Acad Sci U S A*. 1998;95(8):4333–4337.
28. Kawai M, et al. A circadian-regulated gene, Nocturnin, promotes adipogenesis by stimulating PPAR-γ nuclear translocation. *Proc Natl Acad Sci U S A*. 2010;107(23):10508–10513.
29. Xue Y, et al. GPS-SNO: computational prediction of protein S-nitrosylation sites with a modified GPS algorithm. *PLoS One*. 2010;5(6):e11290.
30. Tontonoz P, Hu E, Spiegelman BM. Stimulation of adipogenesis in fibroblasts by PPARγ2, a lipid-activated transcription factor. *Cell*. 1994;79(7):1147–1156.
31. McCauley LK. c-Maf and you won't see fat. *J Clin Invest*. 2010;120(10):3440–3442.
32. van't Hof RJ, Ralston SH. Cytokine-induced nitric oxide inhibits bone resorption by inducing apoptosis of osteoclast progenitors and suppressing osteoclast activity. *J Bone Miner Res*. 1997;12(11):1797–1804.
33. Wimalawansa SJ, De Marco G, Gangula P, Yallampalli C. Nitric oxide donor alleviates ovariectomy-induced bone loss. *Bone*. 1996;18(4):301–304.
34. Engeli S, et al. Regulation of the nitric oxide system in human adipose tissue. *J Lipid Res*. 2004;45(9):1640–1648.
35. Bakker AD, et al. Endothelial nitric oxide synthase is not essential for nitric oxide production by osteoblasts subjected to fluid shear stress in vitro. *Calcif Tissue Int*. 2013;92(3):228–239.
36. Ralston SH, Ho LP, Helfrich MH, Grabowski PS, Johnston PW, Benjamin N. Nitric oxide: a cytokine-induced regulator of bone resorption. *J Bone Miner Res*. 1995;10(7):1040–1049.
37. Aguirre J, et al. Endothelial nitric oxide synthase gene-deficient mice demonstrate marked retardation in postnatal bone formation, reduced bone volume, and defects in osteoblast maturation and activity. *Am J Pathol*. 2001;158(1):247–257.
38. Ahmadian M, et al. PPARγ signaling and metabolism: the good, the bad and the future. *Nat Med*. 2013;19(5):557–566.
39. Martinez-Ruiz A, Lamas S. S-nitrosylation: a potential new paradigm in signal transduction. *Cardiovasc Res*. 2004;62(1):43–52.
40. Taneja G, Mahadevan N, Balakumar P. Fish oil blunted nicotine-induced vascular endothelial abnormalities possibly via activation of PPARγ-eNOS-NO signals. *Cardiovasc Toxicol*. 2013;13(2):110–122.
41. Freise C, et al. (+)-Episesamin inhibits adipogenesis and exerts anti-inflammatory effects in 3T3-L1 (pre)adipocytes by sustained Wnt signaling, down-regulation of PPARγ and induction of iNOS. *J Nutr Biochem*. 2013;24(3):550–555.
42. Berendji D, Kolb-Bachofen V, Zipfel PF, Skerka C, Carlberg C, Kroncke KD. Zinc finger transcription factors as molecular targets for nitric oxide-mediated immunosuppression: inhibition of IL-2 gene expression in murine lymphocytes. *Mol Med*. 1999;5(11):721–730.
43. Kroncke KD, Kolb-Bachofen V. Measurement of nitric oxide-mediated effects on zinc homeostasis and zinc finger transcription factors. *Methods Enzymol*. 1999;301:126–135.

44. Uy HL, et al. Effects of parathyroid hormone (PTH)-related protein and PTH on osteoclasts and osteoclast precursors in vivo. *Endocrinology*. 1995;136(8):3207–3212.
45. Wetmore JB, et al. Elevated FGF23 levels are associated with impaired calcium-mediated suppression of PTH in ESRD. *J Clin Endocrinol Metab*. 2011;96(1):E57–E64.
46. Zhang H, et al. Klotho is a target gene of PPAR-γ. *Kidney Int*. 2008;74(6):732–739.
47. Liu L, et al. Essential roles of S-nitrosothiols in vascular homeostasis and endotoxic shock. *Cell*. 2004;116(4):617–628.
48. Fonseca TL, et al. Double disruption of α2A- and α2C-adrenoceptors results in sympathetic hyperactivity and high-bone-mass phenotype. *J Bone Miner Res*. 2011;26(3):591–603.
49. Dragunow M, Cameron R, Narayan P, O'Carroll S. Image-based high-throughput quantification of cellular fat accumulation. *J Biomol Screen*. 2007;12(7):999–1005.
50. Chandra V, et al. Structure of the intact PPAR-γ-RXR- nuclear receptor complex on DNA. *Nature*. 2008;456(7220):350–356.